Advances in Nano Research, *Vol. 12, No. 2 (2022) 151-165*
https://doi.org/10.12989/anr.2022.12.2.151

Exploring precise deposition and influence mechanism for micro-scale serpentine structure fiber

Han Wang[1,2a], Weicheng Ou[1,2], Huiyu Zhong[2], Jingfan He[1,2], Zuyong Wang[**4], Nian Cai[1,2], XinDu Chen[1,2], Zengxi Xue[1,2], Jianxiang Liao[3], Daohua Zhan[1,2], Jingsong Yao[1,2] and Peixuan Wu[*1,2]

[1]*State Key Laboratory of Precision Electronic Manufacturing Technology and Equipment, Guangdong University of Technology, Guangzhou 510006, P.R. China*
[2]*Guangdong Provincial Key Laboratory of Micro-Nano Manufacturing Technology and Equipment, Guangdong University of Technology, Guangzhou 510006, P.R. China*
[3]*Guangdong Foshan Nanofiberlabs Co., Ltd, Foshan 528000, P.R. China*
[4]*College of Materials Science and Engineering, College of Biology, Hunan University, Changsha 410072, P.R. China*

(*Received June 27, 2021, Revised October 21, 2021, Accepted November 11, 2021*)

Abstract. Micro-scale serpentine structure fibers are widely used as flexible sensor in the manufacturing of micro-nano flexible electronic devices because of their outstanding non-linear mechanical properties and organizational flexibility. The use of melt electrowriting (MEW) technology, combined with the axial bending effect of the Taylor cone jet in the process, can achieve the micro-scale serpentine structure fibers. Due to the interference of the process parameters, it is still challenging to achieve the precise deposition of micro-scale and high-consistency serpentine structure fibers. In this paper, the micro-scale serpentine structure fiber is produced by MEW combined with axial bending effect. Based on the controlled deposition of MEW, applied voltage, collector speed, nozzle height and nozzle diameter are adjusted to achieve the precise deposition of micro-scale serpentine structure fibers with different morphologies in a single motion dimension. Finally, the influence mechanism of the above four parameters on the precise deposition of micro-scale serpentine fibers is explored.
Keywords: axial bending effect; melt electrowriting; precise deposition; serpentine structure

1. Introduction

Flexible electronic integration technology is an emerging electronic technology that integrates organic and inorganic electronic components on flexible substrates. Since flexible electronic functional devices can produce deformation, they have the advantages of greater flexibility and stronger environmental adaptability (Choi *et al*. 2015, Nag *et al*. 2017, Huang *et al*. 2019, Gao *et al*. 2019, Chinnappan 2017). At present, micro-scale serpentine structure fibers have been widely used in the manufacture of biological micro-nano functional devices and flexible electronic devices due to their nonlinear mechanical properties and tissue flexibility (Huang *et al*. 2019, Huang *et al*. 2016). For example, the micro-scale serpentine structure fiber has good tensile and elongation properties, and has been used to make artificial dura substitute (Matsumoto *et al*. 2019) and biomicro-nano sensor with serpentine microstructure (Huang *et al*. 2017) for the treatment of brain tissue damage and other diseases. In addition, micro-scale fibers can be combined with conductive materials such as graphene or nano silver wire conductive solution, used as a carrier to transmit strain information to form a flexible strain sensor (Huang *et al*. 2016, 2021), which can detect deformation in a microscopic state. In the future, with the development of electronic information technology, micro-scale serpentine structure fibers will be widely used in the production of supercapacitors (Kou *et al*. 2014), flexible conductive carriers (Dhanawansha 2020), flexible electronic memory materials (Zhang *et al*. 2019) and other flexible electronic rigid-demand devices. Due to the excellent mechanical flexibility and the conductive properties of combined electrospinning conductive materials, which will lead to higher requirements for the manufacturing technology of micro-scale serpentine structure fibers for flexible sensors, it's practically necessary to explore the influence mechanism of precise deposition about micro-scale serpentine fibers in various process parameters.

As far as the existing serpentine structure preparation technology is concerned, electron beam lithography (Duan *et al*. 2008), focussed ion beam milling (Romagnoli *et al*. 2020), dip-pen nanolithography (Wu *et al*. 2011) can produce micro-nano serpentine, wave and curly pattern. However, due to the disadvantages of low manufacturing efficiency and complex process (Ramakrishna *et al*. 2006, Persano *et al*. 2015), the above-mentioned technology has not been widely used in actual production. As an effective and reliable deposition mode, inkjet printing technology can be used for the deposition of micro-scale serpentine droplets. But the process limit of jet printing size, it hinders the development of more micro-scale serpentine structures

*Corresponding author, Ph.D.,
E-mail: peixuan@gdut.edu.cn
**Co-corresponding author, Professor,
E-mail: wangzy@hnu.edu.cn
[a] Professor, E-mail: wanghangood@126.com

Copyright © 2022 Techno-Press, Ltd.

ISSN: 2287-237X (Print), 2287-2388 (Online)

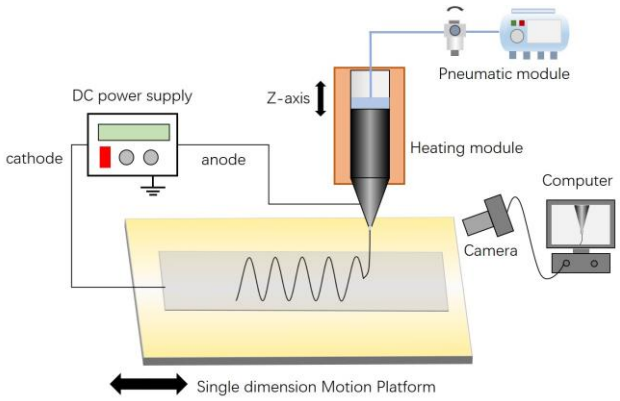

Fig. 1 Schematic diagram of serpentine-direct-writing

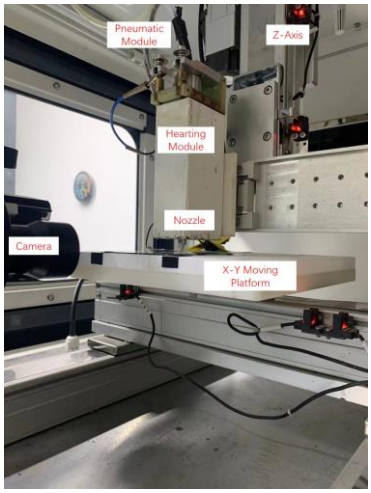

Fig. 2 Diagram of MEW device

manufacture (Fang *et al*. 2015, Duan *et al*. 2017, Nayak *et al*. 2019). In summary, there is an essential to find a simpler, more continuous, and more economical process for the manufacture of serpentine structure fibers. At the same time, it is still necessary to solve the problem of precise deposition of micro-scale serpentine structure fibers in the manufacturing process.

Melt electrowriting (MEW) technology combined with the axial bending effect can make the jet spontaneously generate a serpentine structure, and achieve the precise deposition of the serpentine structure fiber. MEW uses high-temperature molten polymer to electrowriting, which based on electrohydro-dynamics to stably produce micro-nano fibers (Nezadi *et al*. 2021, Wang *et al*. 2021, Zhang *et al*. 2017, 2021, Baji and Abtahi 2013). The axial bending effect comes from the competition between the axial compression and bending of the fluid. The viscous fluid moves down to a stationary surface from a certain height, and a spiral structure jet is generated near the stationary surface. When the stationary surface starts to move, there are several conventional deposition forms such as cycloid and wavy (Kong *et al*. 2016, Passieux *et al*. 2015). In recent years, combined with the rope winding effect characteristics of the sticky body, a stable serpentine or helical structure fiber can be obtained by controlling the process parameters. For example, the spiral hollow fiber membrane is manufactured by adjusting melt extrusion speed, nozzle height or other parameters in the air gap spinning process, which can be applied in adsorption process and wastewater treatment (Luelf *et al*. 2016). Using PEO to adjust the nozzle height and applied voltage in the electrospinning process to produce helical structure fiber (Shariatpanahi *et al*. 2016). Using PVDF to print serpentine fibers with the electrohydrodynamic printing by adjusting applied voltage, spinning distance and other parameters which can be applied in the manufacture hyper stretchable self-powered sensors (Huang *et al*. 2017). Using the PVA to adjust the nozzle height and material viscosity in the FDM process to manufacture spiral micro-fluidic channels with circular cross-sections, which can be appiled in the manufacture of flexible electronic devices (Yang *et al*. 2017). The phenomenon of axial bending has been widely studied and used in the process of serpentine structure. In previous research, it was shown that multiple parameters such as nozzle height, diameter, and collector speed will affect the axial bending effect. In view of the combined existence of electric and gravitational fields in the MEW, the influence of the parameters of micro-scale serpentine fiber forming on its morphology and mechanism are still unclear. In order to improve the manufacture and application of micro-scale serpentine structure fibers, we design single-factor and multiple coupling factors experiments to explore the influence mechanism and precise deposition of micro-scale serpentine structure fibers in four parameters: applied voltage, collector speed, nozzle height and nozzle diameter.

2. Experiment

2.1 Experimental design

In the experiment, polycaprolactone (PCL) particles is used. PCL has the advantages of low melting point, good biocompatibility, and shape memory function. PCL have a melting point of 59-64°C and an average molecular weight of 80,000 (China, Shanghai, Aladdin). It was placed in an environment of 100°C and heated for 30 minutes to turn it into a melt.

The air pressure in the syringe is adjusted to 10 kPa by the air pressure module (China, Shanghai, Jiangyun Instrument Co., Ltd.) to keep the air pressure in the syringe cavity constant. The syringe consists of a 304 stainless steel barrel (specification: 30CC, the inner diameter of the glue outlet: 2mm) and a Musashi precision nozzle (five models 10#, 15#, 20#, 25#, 30#).

The micro-nano fiber collector is fixed on a motion module with a single motion dimension, and indium tin oxide (ITO) glass is used as the receiving matrix of the micro-nano fiber (conductive surface is 50×50 mm square, thickness 1.0 mm). The DC power supply (China, Tianjin, DW-P403, Dongwen Inc) provides DC high voltage between the two poles. It uses different types of stainless steel nozzles as the anode and the ITO glass sheet of the collector as the cathode. An image measuring instrument (China, Dongguan, Rational VMS-3020H) was used to monitor the experimental process.

The schematic diagram of this experimental device and the diagram of MEW device are shown in the Figs. 1 and 2.

Table 1 Main parameter settings of material modeling

	Copper	Glass	PCL	Air
Relative permittivity	2	4.2	2.6	1
Dnsity (kg/m³)	8940	2210	1.5e-3	1.29
Young's modulus (Pa)	126e9	55e9	3.0e6	-
Poisson's ratio	0.34	0.25	0.35	-
Temperature(K)	293.15	293.15	383.15	293.15

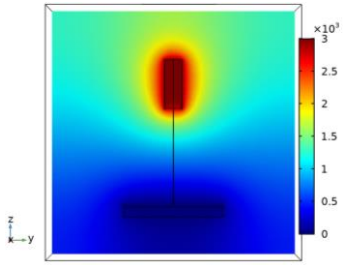

(a)

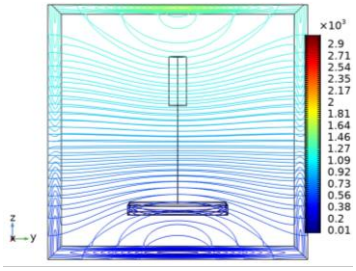

(b)

Fig. 3 Electric potential distribution simulation results

Next, we carry out single-factor experiments and multi-coupling factor experiments to explore the influence mechanism of the above process parameters on serpentine fibers precise deposition by melt electrowriting (MEW).

2.2 Simulation

The finite element simulation software is used to simulate and analyze the MEW axial bending process. First, the MEW device is modeled, with 2 mm as the base the nozzle height, the jet diameter set to vary from 5-10 μm, and the length set to 2 mm. The two ends of the applied voltage electrode coincide with the bottom surface of the nozzle and the top surface of the collector respectively, and the voltage can be set in the range of 2.0 kV to 3.5 kV and the simulation environment set in 25℃. Material modeling is carried out according to the characteristics of the Young's modulus change of the jet material. The material modeling parameter settings are shown in Table 1. After the modeling is completed, analyze the characteristics of the electric potential and electric field distribution in the simulation process. Take the nozzle potential equal to 3 kV as an example to obtain the distribution diagram of Electric potential (Fig. 3(a)), the contour map of potential distribution (Fig. 3(b)), the distribution diagram of the electric field (Fig. 4(a)), the contour map of electric field distribution (Fig. 4(b)) and the electric field distribution trend graph (Fig. 4(c)) are basically consistent with the expected electric field distribution in MEW experiment.

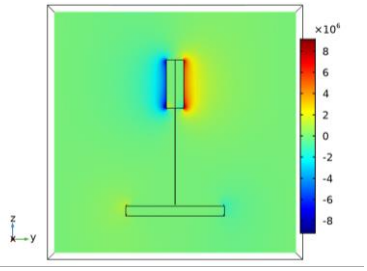

(a) Distribution diagram of the electric field

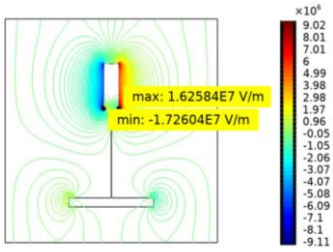

(b) Contour map of electric field distribution

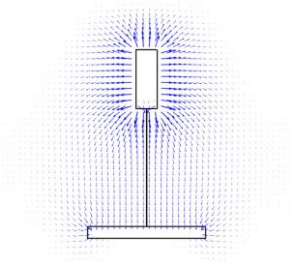

(c) Electric field distribution trend graph

Fig. 4 Simulation results of electric field intensity vector distribution

Table 2 The total displacement measured by the jet flow domain probe at different time nodes

Time (s)	Total displacement of jet domain probe (mm)
0.0000	1.86×10^{-10}
0.010000	9.78×10^{-4}
0.020000	1.86×10^{-3}
0.030000	3.80×10^{-3}
0.040000	0.56×10^{-2}
0.050000	1.22×10^{-1}

Subsequently, the bending process of the jet is simulated by electric field coupling. The time and step size set in simulation are range (0, 0.01, 0.1), the time step is 0.004s. The series of simulation results obtained are shown in Fig. 5. It can be seen that the bending morphology of the jet has changed significantly over time. The obvious change of the total displacement also shows that the electric field has a continuous effect on the bending of the jet, and the different forms of bending structure can be deposited. Setting the domain probe on the jet and observing the total displacement of each main time node in 0.05 s. The measured displacement values are shown in Table 2. It can be found that the total displacement of the jet in a period is different. The change curve of the maximum displacement measured by the jet domain probe in 0~0.1s is shown in Fig. 6(a). It

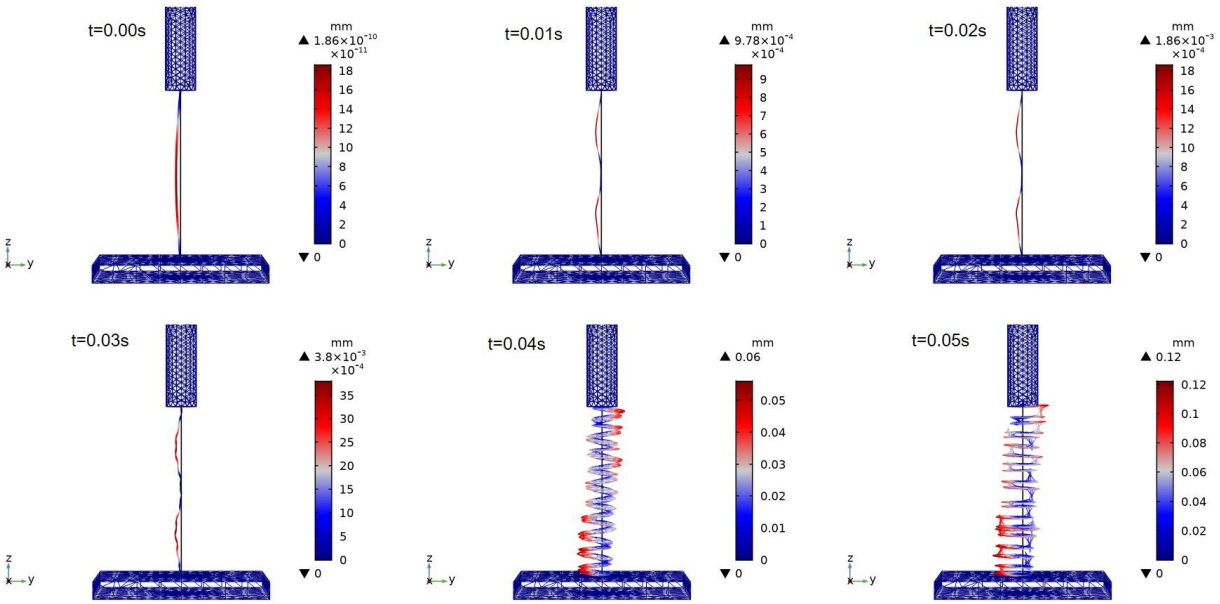

Fig. 5 Deformation of jet at several typical moments in 0.00-0.05 s

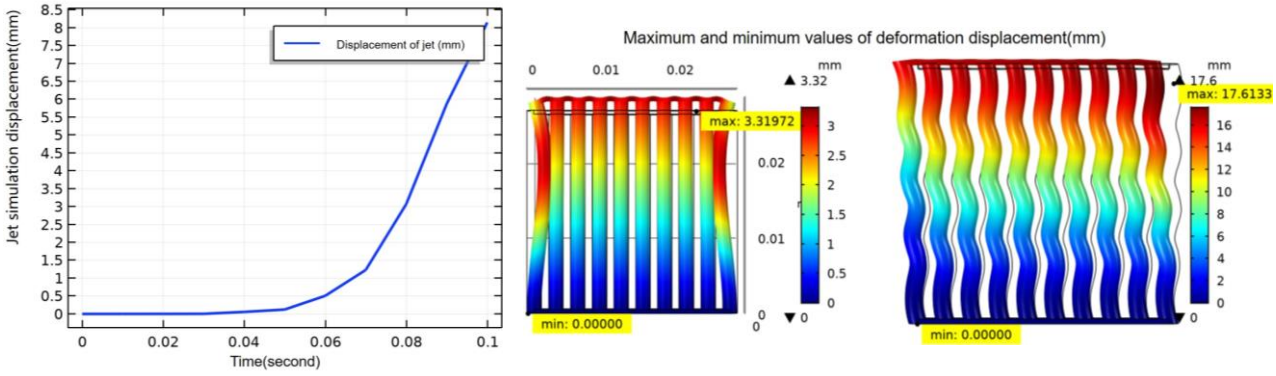

(a)Integral change curve of total displacement measured

(b) Deformation simulation of serpentine structure

Fig. 6 Integral change curve of total displacement measured by jet domain probe and deformation simulation results of serpentine structure

can be clearly observed that the jet displacement gradually increases under the continuous action of the electric field force. The maximum displacement increases from 1.86×10^{-10} mm at the beginning to 8.5 mm at 0.1 s, which basically maintains a linear increase within 0.1 s and also proves that the electric field influence the displacement of the jet. Analysis of the stiffness coefficient of the three-dimensional serpentine structure and the stress distribution under load showed that the deformability of the three-dimensional serpentine microstructure is better than that of the linear three-dimensional microstructure Fig. 6(b). It shows the feasibility and great potential of three-dimensional serpentine structure in flexible device manufacturing.

The above simulation results show that the existence of the electric field influences the jet's axial bending effect, and it is feasible to control the formation of micro-scale serpentine fibers by applying an electric field. The simulation results are necessary for the micro-scale serpentine structure fibers through the NEW process.

3. Results and discussion

3.1 Single-factor experiment

In this single factor experiment, the pressure setting is set to 10 kPa and the melting module temperature setting is to 110°C.

3.1.1 The influence of nozzle diameter

In the process of melt electrowriting (MEW), according to Eq. (1), when the jet radius (r) from the Taylor cone changes, it will have a significant impact on the jet mass (m). Under the other external conditions remain same, the jet will have an unstable rotational motion when it is falling, so the rotation velocity (v) of the jet around the central axis will also change. According to Eq. (2), the force (F_{force}) of jets with different diameters can be obtained within the same time (t).

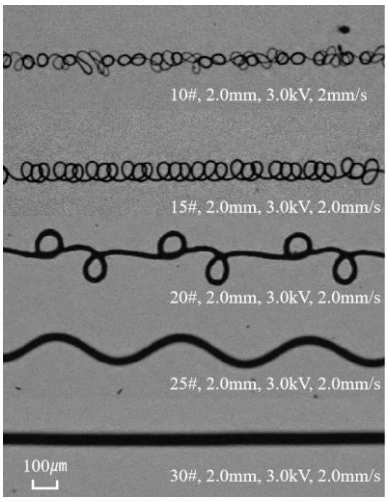

Fig. 7 Serpentine deposition obtained by different nozzles

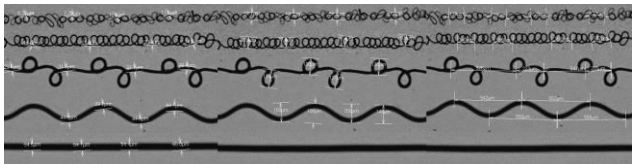

(a)

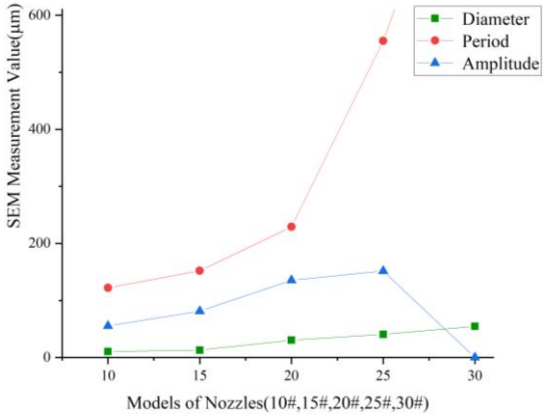

(b)

Fig. 8 (a) Part of the measurement data of serpentine diameter, period and amplitude; (b) Variation curves of serpentine fiber parameters of different nozzles

$$m = \rho r^3 h \tag{1}$$

$$F_{force} t = mv \tag{2}$$

Within the same time (t), the jet radius (r) becomes larger and the jet mass (m) becomes larger. The external force (F_{force}) remains unchanged, and the velocity (v) will increase significantly, which leads to more obvious bending of the jet in space, thereby obtaining a larger bending radius. Therefore, the diameter change of the jet will have a significant impact on the axial bending effect.

The parameter controlled by the group of experiments is the nozzle models, different nozzle models represent different nozzle inner diameters. The nozzles models of 10#, 15#, 20#, 25#, and 30# respectively correspond to the inner diameters of 100 μm, 150 μm, 200 μm, 250 μm, 300 μm.

Table 3 The measurement average of four sets of repetitive experiments

Fiber Diameter				
10#	15#	20#	25#	30#
10.4	12.9	30.3	40.5	54.6
Fiber Period				
10#	15#	20#	25#	30#
122.3	152.8	227.5	549.8	+∞
Fiber Amplitude				
10#	15#	20#	25#	30#
55.4	81.2	135.4	151.8	0

Set nozzle height to 2 mm, collector speed to 2 mm/s, and applied voltage to 3.0 kV. After the parameters are determined, the experimental results obtained are shown in Fig. 7.

It can be observed from Fig. 7 that the fibers of 10# nozzles are very messy and disordered which the specific morphology is still unclear at 100 magnification. The fibers of 15# nozzles begin to become orderly, but it is difficult to obtain stable deposition. The fibers of 20# nozzles appeared stable and orderly spiral buckling morphology, and the deposition began to become stable. The fibers of 20# nozzles became more orderly and began to appear stable serpentine deposition. Finally, the deposited fibers of the 30# nozzle had no axial bending to obtain a straight line. From the qualitative analysis of the above situation, the diameter of the nozzle has an influence on the deposition of serpentine fibers. Under the same electric field condition and the collector speed, larger inner diameter of the nozzle makes larger Taylor cone, and the greater electric field force is required for the jet to break through the surface tension of the Taylor cone. After the jet breaks through the Taylor cone, the mass of the jet unit is larger in the axial direction, and the influence of the electric field force on the jet's axial bending effect is weaker. Because the inner diameter of 10# and 15# nozzles is too small and the mass of the jet unit in the axial direction is also small, the deposited fibers obtained are disordered and messy. In the same way, the jet unit of the 30# nozzle in the axial direction has a larger mass, and the deposited fiber obtained is only a straight line.

After completing the qualitative analysis, this article will design four groups of reproducible experiments to quantitatively analyze the fiber diameter, serpentine amplitude and period. Keep the above parameters unchanged and print four sets of data respectively as shown in the Table 3. In each set of data, four points are randomly selected as measurement points, and the invalid data of the measurement results are removed and the average value is taken, as shown in the Fig. 8(a). Finally, using the inner diameter of the nozzle as the abscissa, the change curves of fiber diameter, serpentine period and serpentine amplitude are made as shown in Fig. 8(b).

In summary, the deposition morphology of serpentine fibers doesn't show much deviation under the same parameters. Different models of nozzles have completely

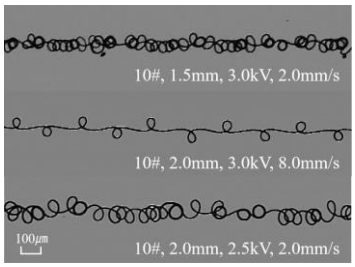

Fig. 9 The serpentine fibers obtained by reducing nozzle heights, increasing collector speed and reducing applied voltage with the 10# nozzle

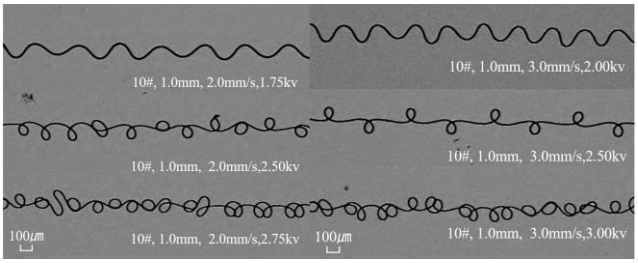

Fig. 10 The obtains controlled serpentine deposition when the nozzle at 1 mm with 10# nozzle

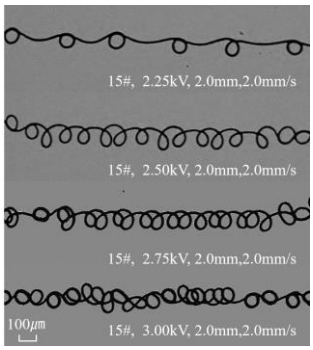

(a) The experimental results of the voltage drop when the 15# nozzle height is 2 mm

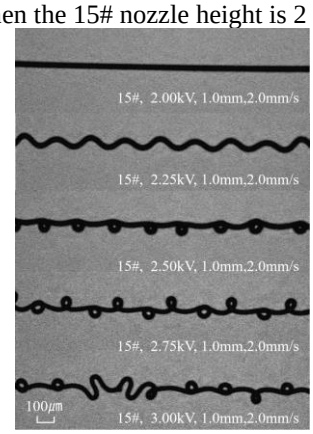

(b) The experimental results of the voltage when the 15# nozzle height is 1 mm

Fig. 11 The experimental results of the 15# nozzle with different applied voltages

different deposition characteristics under the same parameter, and each nozzle to obtain controlled serpentine structure deposition needs to individually explore the parameter range. The diameter of the fiber becomes larger as the diameter of the nozzle becomes larger. The period becomes larger as the diameter of the nozzle becomes larger and the period gradually becomes larger to infinity. The serpentine amplitude first becomes larger gradually becomes smaller to zero as the nozzle diameter becomes larger. The average amplitude measured in the experiment includes the diameter of the fiber. When analyzing the amplitude of the serpentine deposition, it is inevitable to consider the influence of the fiber diameter. Therefore, the following experiment will only discuss the serpentine amplitude.

In the experiment, it was found that the serpentine deposits of 10# and 15# nozzle are disordered, which means that the nozzle inner diameter is too small and causes the applicable range of controlled deposition to be very different from the other nozzle (20#, 25#, 30#). Next, the situation of 10# and 15# nozzle were explored separately.

10# nozzles obtain different morphology of bending under the combination of different applied voltage, different nozzle height and different collector speed. As shown in Fig. 9, When nozzle height is fixed at 1.5 mm, the morphology of the fiber is still very disordered and messy, indicating that it still very difficult to achieve controllable serpentine fibers by adjusting the nozzle height. Then, ensuring nozzle height is fixed at 2.0 mm and applied voltage of 3.0 kV, collector speed was gradually increased. Finally, it was found that the deposition of serpentine fibers became orderly and controllable when collector speed reached 8 mm/s. With the same nozzle height and collector speed, when applied voltage is reduced to 2.5 kV, it is found that the deposition of serpentine fibers is still disordered, which shows that applied voltage reduce is still not enough to make the deposition of serpentine fibers correctly. Then lower nozzle height to 1.0 mm as shown in Fig. 10, when collector speed is 1 mm/s, orderly serpentine fibers cannot be obtained. At collector speed of 2 mm/s, controllable serpentine fibers can be obtained in the range of applied voltage 1.75 kV to 2.75 kV. When collector speed is 3 mm/s, applied voltage is within the range of 2.0 kV to 3.0 kV to obtain controllable serpentine fibers. When collector speed reaches 4 mm/s, controllable serpentine fibers can't be obtained; only linear fibers can be obtained. From the experimental results, it is difficult to obtain stable and controllable serpentine fibers with a 10# nozzle under the condition of parameters. Therefore, the following article will not explore the 10# nozzle.

15# nozzle at nozzle height of 2.0 mm and collector speed is 2 mm/s, applied voltage is reduced at 0.25 kV intervals, and the fiber morphology is finally obtained, as shown in Fig. 11(a). When applied voltage was adjusted to 2.25 kV, the fiber began to deposit. When applied voltage is increased to 2.75 kV, it is difficult to find an orderly serpentine fibers morphology, which indicates that it is difficult to obtain controlled deposition with the 15# nozzle under this parameter setting. Lower nozzle height to 1.0 mm and fix it, continue to set collector speed to 2 mm/s, and then continue to experiment. The result is shown in Fig. 11(b).

The experimental results in the Fig. 11 show that applied voltage range of the controllable serpentine fibers of the 15# nozzle is from 2.25 kV to 2.75 kV.

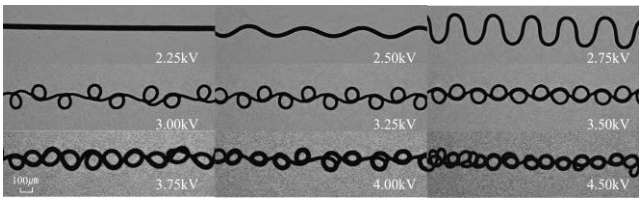

(a) Serpentine deposition with different voltages under 20# nozzle

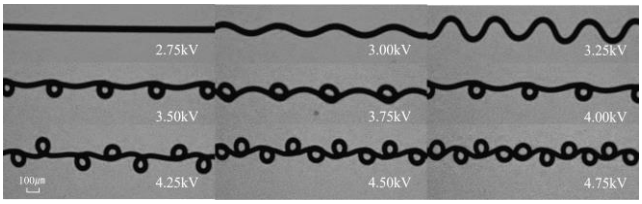

(b) Serpentine deposition with different voltages under 25# nozzle

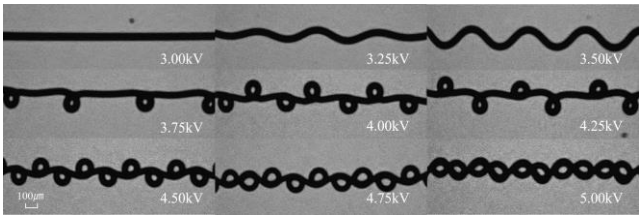

(c) Serpentine deposition with different voltages under 30# nozzle

Fig. 12 The serpentine deposition change under different applied voltages of three models nozzles

A series of experiments show that it is difficult to obtain controllable serpentine fibers with the 15# nozzle and the parameter range of its controllable deposition is relatively small. Therefore, the following experiment will not explore the 15# nozzle.

3.1.2 The influence of applied voltage

Applied voltage is mainly to change the magnitude and direction of the electric field force by changing the magnitude and distribution of the electric field strength. The magnitude and direction of the electric field force affects the jet falling velocity and the axial bending effect of the jet. According to Eq. (3):

$$E = U_{AV}/H_{NH} \tag{3}$$

U_{AV} represents the value of applied voltage, H_{NH} represents the height from the nozzle to the collector. The magnitude of the electric field strength (E) mainly depends on applied voltage and nozzle height. nozzle height remains unchanged, the greater applied voltage, the greater the electric field force, the more obvious the stretching effect on the jet, and the longer the length of the jet falling straight. During MEW, because the distance between the nozzle and the collector is very close, the selection of electric field force must also find a suitable range. Too weak electric field force can not cause the jet to break through the surface tension of the Taylor cone, and too large electric field force will make the jet straight, which directly exceeds the height of the axial bending effect, making the jet too late to produce the axial bending effect.

In this part, 20#, 25#, 30# nozzles are selected for the experiment. nozzle height is set to 2 mm and collector speed is set to 2 mm/s. The single factor controlled in this experiment is applied voltage value. applied voltage is set from 2.0 kV to 5.0 kV, the voltage value interval is 0.25 kV, and the result is shown in Fig. 12.

From Figs. 12(a)-12(c), it can be seen that the voltage range of the controllable morphology of serpentine fibers under 20# nozzle is 2.50 kV-4.00 kV. Under applied voltage and collector speed remain unchanged, the 20# nozzle begins to deposit orderly and obtain wave-shaped fibers when applied voltage is 2.5 kV. When value increases to 2.75 kV, the morphology is still wavy. When applied voltage increased to 3.0 kV, the deposition morphology began to appear spiral, and the voltage value continued to increase, and the deposition morphology began to slowly change to “8” or “inverted “8”shapes. Until the voltage increased to 4.0 kV, the deposition morphology began to become disordered. The change of deposit morphology of 25# and 30# nozzles is similar to that of 20# nozzles. But the voltage range of the controllable morphology of the deposition under the 25# nozzle is from 3.0 kV to 4.75 kV, and the voltage range of the controllable morphology of the deposition under the 30# nozzle is increased to the range of 3.25 kV to 5.0 kV.

Keep the above parameters unchanged, and design four groups of reproducible experiments to quantitatively analyze the serpentine amplitude and period. In each set of data, four points are randomly selected as measurement points, the measurement results are removed after invalid data and the average value is taken, as shown in the Table 4. The period and amplitude of the serpentine fibers obtained

Table 4 The measurement average of four sets of repetitive experiments

Fiber amplitude (“-” means the fiber morphology is messy and difficult to measure)					
20#		25#		30#	
2.25 kV	0.0	2.75 kV	0.0	3.00 kV	0.0
2.50 kV	54.7	3.00 kV	58.6	3.25 kV	61.0
2.75 kV	122.2	3.25 kV	103.4	3.50 kV	98.0
3.00 kV	130.6	3.50 kV	134.5	3.75 kV	165.3
3.25 kV	128.5	3.75 kV	135.2	4.00 kV	161.2
3.50 kV	129.3	4.00 kV	135.4	4.25 kV	161.6
3.75 kV	-	4.25 kV	133.7	4.50 kV	164.8
4.00 kV	-	4.50 kV	-	4.75 kV	-
Fiber period (“-” means the fiber morphology is messy and difficult to measure)					
20#		25#		30#	
2.25 kV	+∞	2.75 kV	+∞	3.00 kV	+∞
2.50 kV	882	3.00 kV	862	3.25 kV	948
2.75 kV	592	3.25 kV	739	3.50 kV	869
3.00 kV	423	3.50 kV	771	3.75 kV	1043
3.25 kV	348	3.75 kV	483	4.00 kV	651
3.50 kV	322	4.00 kV	357	4.25 kV	548
3.75 kV	-	4.25 kV	336	4.50 kV	361
4.00 kV	-	4.50 kV	-	4.75 kV	-

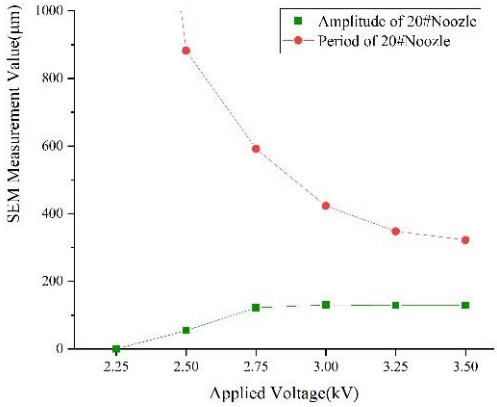

(a) Serpentine fibers period and amplitude of 20# Noozle

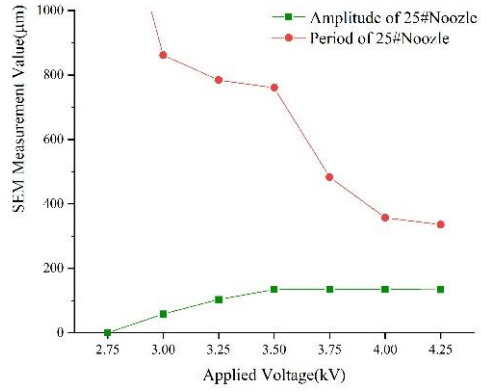

(b) Serpentine fibers period and amplitude of 25# Noozle

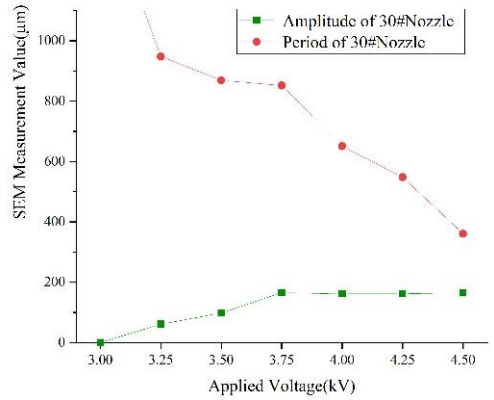

(c) Serpentine fibers period and amplitude of 30# Noozle

Fig. 13 Variation curve of deposition morphology when the applied voltage changes

by 20#, 25#, 30# nozzle are measured and plotted as shown in Figs. 13(a)-13(c).

In summary, the deposition morphology of serpentine fibers does not show much deviation under the same parameters. As the applied voltage increases, the serpentine deposition of each nozzle has a similar trend. The amplitude gradually decreases, and the period basically remains unchanged, which shows that the applied voltage plays a positive role to the period, but does not affect the change of the amplitude. The voltage range of the controllable morphology of serpentine deposition under different nozzles also showed characteristic: the initial voltage of serpentine deposition gradually increases and the voltage of disordered deposition morphology also gradually increases. For example, the initial voltage for the appearance of orderly serpentine deposition morphology gradually increased from 2.5 kV (20#) to 3.25 kV (30#) and the initial voltage for the disordered deposition gradually increased from 4.0 kV (20#) to 5.0 kV (30#). Different nozzles have different voltage ranges for serpentine deposition to obtain a controllable morphology, but the fibers appearance change trend is roughly the same, all of them are gradually evolving from “wave or serpentine” -shaped to “8” or “inverted-8”-shaped.

3.1.3 The influence of the nozzle height

In the melt electrowriting (MEW) process, different nozzle heights will cause the jet to bend axially. The axial bending effect will change the bending frequency and the bending diameter of the jet, resulting in serpentine deposition. Therefore, the selection of the nozzle height also needs a range so that the jet can not only produce the axial bending effect but also obtain different deposition morphologies. As shown by Eq. (3).

In this part, 20#, 25#, 30# nozzles are selected for the experiment. The applied voltage is set to 3 kV, and the collector speed is set to 2 mm/s. The single factor controlled in this experiment is nozzle height. The setting of the nozzle height starts from 1 mm and gradually increases at 0.5 mm intervals until the jet deposition morphology changes from order to disorder. The experimental results are shown in Fig. 14.

Fig. 14(a) shows the deposition morphology obtained with a 20# nozzle. It shows that when the nozzle height is 1 mm, the fiber morphology is the spiral-shape with a smaller serpentine amplitude. It shows that the deposition at this time is a stage of transition from wave-shape fiber to spiral-shape fiber. When the nozzle height is increased to 1.5 mm, the fiber morphology becomes spiral with a larger amplitude. When the nozzle height is increased to 2mm and 2.5 mm, the fiber morphology gradually changed to “8”-shape or “inverted 8”-shape. As the nozzle height increases, the electric field force becomes small enough that it can not longer effectively control the axial bending during the falling process of the jet, so the jet has the whipping phenomenon and disordered deposition. As shown in Figs. 14(b) and 14(c), the morphology of the fibers obtained by 25# and 30# nozzles also basically follows the gradual change from the wave-shape to the “8”-shape or “inverted 8”-shape as the nozzle height increases. At the same time, as the nozzle inner diameter increases (suah as 20#, 25#, 30#), the nozzle height for disorderly deposits should be increased accordingly. Both the 25# and 30# nozzles need to be higher than 3.0 mm before the jet whipping phenomenon and obtain disordered deposition.

For the size and distribution of the electric field, it is not only related to the applied voltage but also to the nozzle height. Under other conditions unchanged, the change of the nozzle height causes the change of the electric field (E) to affect the morphology of the serpentine deposition. Compared to applied voltage, the nozzle height has the opposite effect on the morphology of the serpentine deposition. After clarifying the influence mechanism of the

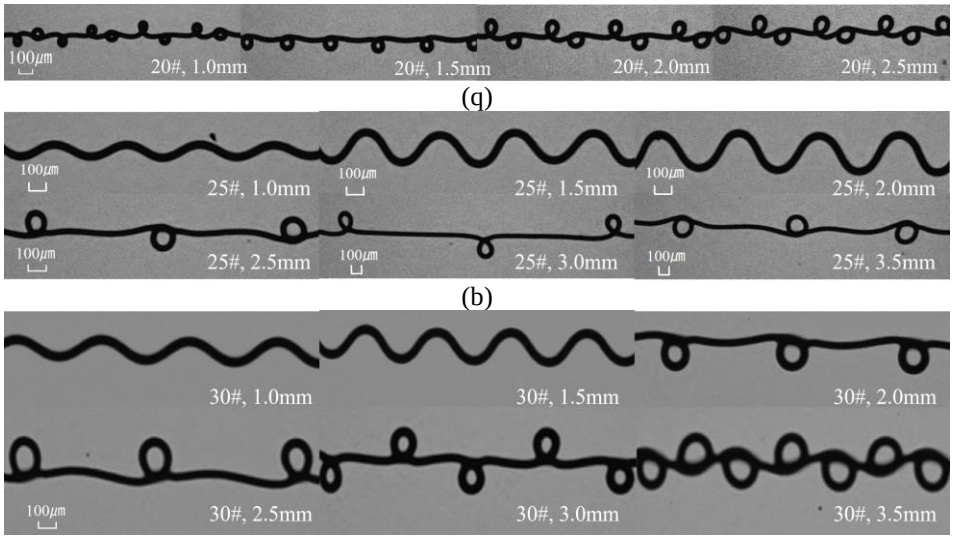

Fig. 14 The Serpentine deposition changes under different nozzle heights of three models nozzles

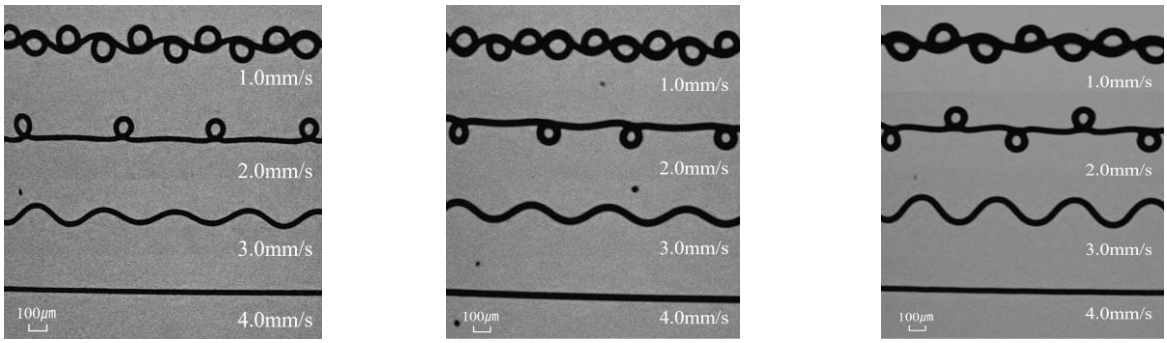

(a) Serpentine deposition under different collector speed of 20# nozzle

(b) Serpentine deposition under different collector speed of 25# nozzle

(c) Serpentine deposition under different collector speed of 30# nozzle

Fig. 15 The Serpentine deposition changes under different collector speed of three models nozzles

applied voltage and the nozzle height on the serpentine fiber deposition, the quantitative analysis of the serpentine period and amplitude was not carried out. Keeping the above parameters unchanged and carrying out repetitive experiments, the change trend of the fiber along with the change of the nozzle height is basically consistent with the above qualitative analysis.

In summary, with other conditions unchanged, the change of the nozzle height affects the morphology of the serpentine. As the nozzle height increases from 1.0 mm to 3.5 mm, the fiber morphology first changes from wave-shape to spiral-shape to "8" or "inverted 8"-shape, and finally to obtain disordered deposition. In addition, as the inner diameter of the nozzle increases, the height of the nozzle where the disordered deposited fibers appear is also higher, such as the 25# nozzle and 30# nozzle.

3.1.4 The influence of collector speed

Collector movement will drag the jet before it falls on the collector, and this drag effect and axial bending effect of the jet will cancel each other out, so that collector speed will have a greater impact on the deposition of the jet. The greater the collector speed, the weaker the jet axial bending effect and the less obvious the bending of the deposition. The collector will have a drag effect on the jet in the same direction. The drag force F_{drag} is proportional to collector speed (*Vcs*), and the relationship can be expressed as Eq. (4):

$$F_{drag}=k_i V_{cs} \tag{4}$$

The constant k_i relates to the quality and volume of collector. With the increasing of collector speed, its drag force on the jet will definitely increase. When the velocity becomes very high, the drag force will also be very large, which will increase the straight falling distance of the jet and the jet will not have time to make a reaction on the axial direction so that the serpentine structure cannot be produced. It makes the collector speed directly affect the morphology of the jet.

In this part, 20#, 25#, and 30# nozzles are selected for the experiment. The nozzle height is set to 2 mm. The collector speed is set from 1 mm/s to 4 mm/s. During the experiment, the collector speed was gradually increased, until the jet deposition morphology was completely straightened. The experimental results obtained are shown in Fig. 15.

Table 5 The measurement average of four sets of repetitive experiments

	Fiber Amplitude			Fiber Period		
	20#	25#	30#	20#	25#	30#
1.0 m/s	151.2	168.7	227.5	350.1	354.2	550.8
1.5 m/s	139.1	163.5	208.4	423.8	436.8	697.4
2.0 m/s	126.1	155.2	175.3	476.3	506.2	797.6
2.5 m/s	82.3	101.3	117.9	621.4	710.9	923.1
3.0 m/s	46.3	58.9	76.9	742.0	863.5	967.2
3.5 m/s	20.6	27.4	38.7	985.0	1676.0	2964.0
4.0 m/s	0.0	0.0	0.0	+∞	+∞	+∞

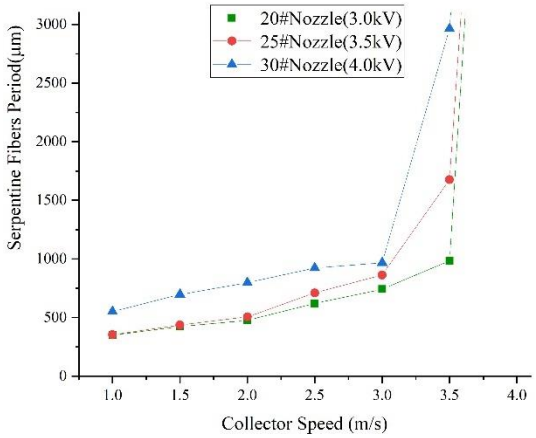

(a) The period under different collector speed of three models nozzles

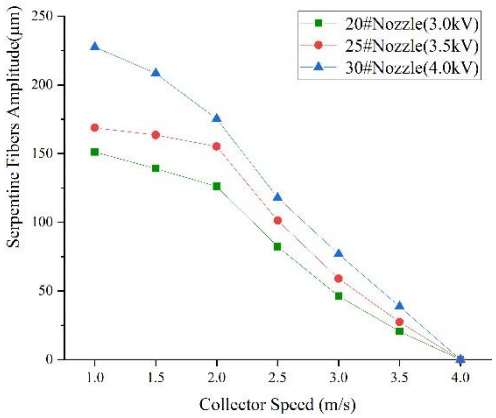

(b) The amplitude under different collector speed of three models nozzles

Fig. 16 Variation curve of deposition morphology when the collector speed changes

As shown in Fig. 15(a), when the applied voltage of the 20# nozzle is 3.0 kV and the nozzle height is 2 mm, the collector speed starts in 1 mm/s can obtain a deposition similar to the “inverted 8”-shape. The morphology of deposition at this time is controllable and orderly. When the collector speed increases to 2 mm/s, the morphology of the deposition is characterized by a spiral type with a larger serpentine period and a smaller amplitude. At this time, the morphology of deposition is also orderly and controllable. When the collector speed increases to 3 mm/s, the deposition morphology becomes wave-shaped, and the drag effect of the collector movement is more obvious at this time. When the speed is increased to 4 mm/s, the fibers are straightened. The speed range of collector with controllable and orderly morphology of serpentine deposition under 20# nozzle is from 1 mm/s to 3 mm/s. Subsequently, the 25# nozzle was tested at a voltage of 3.5 kV and the nozzle height was 2 mm, and the 30# nozzle was tested at a voltage of 4.0 kV and the nozzle height of 2 mm. The results are shown in Figs. 15(b) and 15(c). 25# and 30# nozzles have similar deposition process to 20# nozzles, and the velocity range of the collector with controllable serpentine deposition morphology is 1 mm/s to 3 mm/s.

Table 6 Multi-coupling factors explore experimental parameter settings

Types of nozzles	Parameter Settings	
20#	Alppied Voltage E_1~E_3（kV）	2.5、3.0、3.5
	Collector speed V_{cs1}~ V_{cs3}（mm/s）	1、2、3
25#	Voltage E_1~E_3（kV）	3.0、3.5、4.0
	Collector speed V_{cs1}~ V_{cs3}（mm/s）	1、2、3
30#	Voltage E_1~E_3（kV）	3.5、4.0、4.5
	Collector speed V_{cs1}~ V_{cs3}（mm/s）	1、2、3

Keep the above parameters unchanged and design four groups of reproducible experiments to quantitatively analyze the serpentine amplitude and period. In each set of data, four points are randomly selected as measurement points, the measurement results are removed after invalid data and the average value is taken, as shown in the Table 5. The period and amplitude of the serpentine fibers obtained by 20#, 25#, 30# nozzle are measured and plotted as shown in Figs. 16(a)-16(b).

In summary, the deposition morphology of serpentine fibers does not show much deviation under the same parameters. The serpentine fibers period shows a clear increasing trend with the increase of collector speed and finally becomes infinite when it becomes a straight line. The serpentine fibers amplitude gradually decreases with the increase of collector speed until the fiber is straightened to zero at the end. This shows that when the collector is moving, the drag effect on the jet is in the same direction as the motion. The selection of the collector speed directly affects the shape of the jet that has an axial bending effect. The fiber deposition ranges from “inverted-eight”-shaped to spiral-shaped to serpentine-shaped and finally to linear. In this experiment, when other conditions remain same and the collector speed keep from 1 mm/s to 3 mm/s, all nozzles can obtain serpentine fibers with a controllable and orderly morphology.

3.2 Multiple coupling factors exploring experiment

This experiment will explore the significance of the influence of process factors on the morphology of serpentine structures by setting the variance experiment. According to the Eq. (3), the nozzle height and the applied voltage affect the size of the electric field strength together,

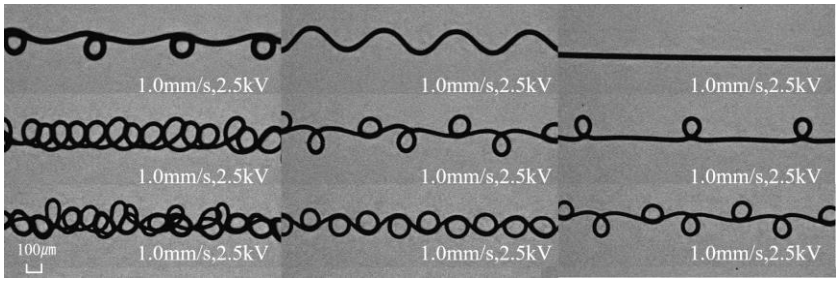

(a) Experiment results under 20# nozzle

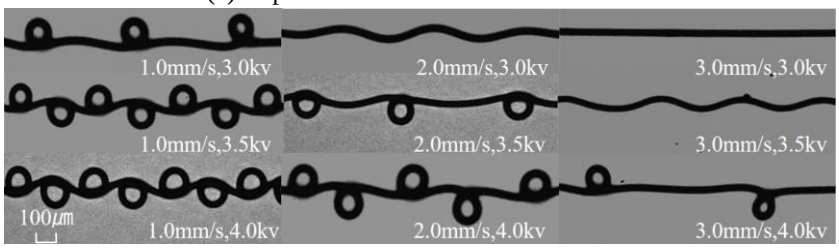

(b) Experiment results under 25# nozzle

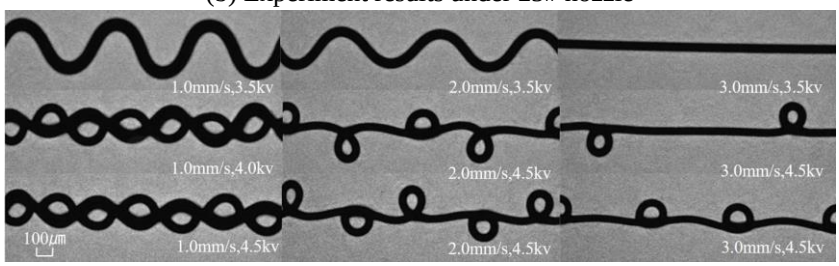

(c) Experiment results under 30# nozzle

Fig. 17 Results of multiple coupling factors experiment

Table 7 Nozzle of 20# two-factor three-level variance experiment expected value measurement results

	Serpentine amplitude (μm)		Serpentine period (μm)	
	Measured value of each group	average value	Measured value of each group	average value
X_{11}	167.19 158.05 160.96 163.95	162.54	500.00 512.95 504.46	505.80
X_{12}	72.54 77.72 72.54 72.54	73.83	490.41 502.23 506.64 502.23	500.38
X_{13}	0	0	∞	∞
X_{21}	169.86 174.39 163.21 170.35	169.45	98.45 129.53 129.53 113.99	117.88
X_{22}	130.46 129.64 132.23 139.99	133.08	549.23 554.41 533.68 557.00	548.58
X_{23}	101.28 107.31 94.72	101.10	1184.97 1231.61	1208.29

Table 7 Continued

	Serpentine amplitude (μm)		Serpentine period (μm)	
	Measured value of each group	average value	Measured value of each group	average value
X_{31}	171.47 174.81 156.82 166.28	167.34	0	0
X_{32}	137.53 139.90 135.11 142.58	138.78	168.39 173.58 165.80 173.58	170.34
X_{33}	99.17 107.18 105.67 102.15	103.54	528.50 536.27 525.91 541.45	533.03

Table 8 Calculation results of two-factor three-level variance experiment of serpentine amplitude

	V_1	V_2	V_3	$T_i = \sum_{j=1}^{3} \mathrm{X}_{ij}$	$\overline{X}_i = T_i/3$
E_1	162.54	73.83	0	236.37	45.46
E_2	169.45	133.08	101.10	403.63	134.54
E_3	167.34	138.78	103.54	409.66	136.55
$T_j = \sum_{i=1}^{3} \mathrm{X}_{ij}$	499.33	345.69	204.64	1049.66	
$\overline{X}_j = T_j/3$	166.44	115.23	68.21		116.63

Table 9 Calculation results of two-factor three-level variance experiment of serpentine amplitude

	V_1	V_2	V_3	$T_i = \sum_{j=1}^{3} \mathrm{X}_{ij}$	$\overline{X}_i = T_i/3$
E_1	505.80	1000.76	2000	3506.56	1168.85
E_2	117.88	548.58	1208.29	1874.75	624.91
E_3	0	170.34	533.03	703.37	234.46
$T_j = \sum_{i=1}^{3} \mathrm{X}_{ij}$	623.68	1719.68	3741.32	6084.68	
$\overline{X}_j = T_j/3$	207.89	573.23	1247.11		676.08

so the applied voltage is chosen to represent the *E* to explore their significance on the deposition morphology. In this experiment, the specific experimental parameters and level factors settings are shown in Table 6.

The nozzle height fixed at 2 mm, and the experiment is carried out with PCL. The experimental results are analyzed according to different models of nozzles, as shown in Fig. 17.

20# nozzles as shown in Fig. 17(a) as an example: when the applied voltage is 2.5 kV, the morphology of the serpentine deposit changes from spiral-shape to wave-shape to straight line with the increase of collector speed. When the applied voltage is set from 3.0 kV to 3.5 kV, the morphology of the serpentine deposition gradually changes from disorder to order with the increase of collector speed. The same qualitative analysis of the experimental results of 25# nozzle and 30# nozzle also showed such an obvious trend. The results of this multi-coupling factor exploration experiment are feasible.

Next, analyze the morphological characteristics of the serpentine deposition according to the period and the amplitude of the serpentine fibers. Design four groups of repetitive experiments, randomly take four points from each group experiment to measure the period and the amplitude of the serpentine morphology and calculate their average value. According to the calculation in Tables 7-9, the

Table 10 Two-factor experiment analysis of variance

Source variance	Sum of square	Degree of freedom	Sum of mean square	*F*	*F* critical value
Voltage variable	S_E	df_E	$MS_E=\frac{S_E}{df_E}$	$F_E=\frac{MS_E}{MS_\varepsilon}$	$F_a((a\text{-}1),(a\text{-}1)(b\text{-}1))$
Velocity variable	S_{Vcs}	df_{Vcs}	$MS_{Vcs}=\frac{S_V}{df_V}$	$F_{Vcs}=\frac{MS_{Vcs}}{MS_\varepsilon}$	$F_b((b\text{-}1),(a\text{-}1)(b\text{-}1))$
Inaccuracy variance	S_ε	df_ε	$MS_\varepsilon=\frac{S_\varepsilon}{df_\varepsilon}$		
Variance	S_T	df_T			

Table 11 The sum of squares and degrees of freedom of the serpentine amplitude variance experiment

Calculate variable value	Sum of square	Degree of freedom
$D_E = 128869.76$	$S_E = D_E - P = 6449.08$	$df_E = 3-1=2$
$D_{Vcs} = 136903.18$	$S_{Vcs} = D_{Vcs} - P = 14482.50$	$df_{Vcs} = 3-1=2$
$P = 122420.68$	$S_\varepsilon = S_T - S_E - S_V = 3145.76$	$df_\varepsilon = 2\cdot 2 = 4$
$R = 146498.02$	$S_T = R - P = 24077.34$	$df_T = 9-1=8$

Table 12 The sum of squares and degrees of freedom of the serpentine amplitude variance experiment

Calculate variable value	Sum of square	Degree of freedom
$D_E = 5435126.65$	$S_E = D_E - P = 1321423.24$	$df_E = 3-1=2$
$D_{Vcs} = 5781250.46$	$S_{Vcs} = D_{Vcs} - P = 1667547.05$	$df_{Vcs} = 3-1=2$
$P = 4113703.41$	$S_\varepsilon = S_T - S_E - S_V = 242617.65$	$df_\varepsilon = 2\cdot 2 = 4$
$R = 7345291.35$	$S_T = R - P = 3231587.94$	$df_T = 9-1=8$

expected value is calculated by measuring the average value of the serpentine period and the serpentine amplitude, and then the expected value is analyzed by variance.

In the analysis of variance, first calculate the experimental error of the mathematical expectation value according to the Eq. (5):

$$\varepsilon_{ij} = X_{ij} - \bar{X} \tag{5}$$

Next, calculate the effect of each level of electric field strength (*E*) on the experimental results according to Eq. (6).

$$\alpha_i = \bar{X}_\iota - \bar{X} \tag{6}$$

Then according to Eq. (7), calculate the effect of each level of collector speed on the experimental results

$$\beta_j = \bar{X}_J - \bar{X} \tag{7}$$

Finally, after completing the calculation of the influence effect on each level, it is found through calculation and verification that the experimental results conform to the linear statistical model Eq. (8) formula:

$$X_{ij} = \bar{X} + \alpha_i + \beta_j + \varepsilon_{ij} \tag{8}$$

It shows that the experimental results are true and effective and the calculation process is correct.

After the data verification is over, the next step is to calculate the sum of squared deviations of the serpentine fiber amplitude and period. According to the calculation formula set in Table 10, the final expected value of the sum of squares and the degree of freedom about the amplitude and period is shown in Tables 11-12:

After the calculation of the sum of mean square is completed, the *F* of each factor can be calculated. The *F* of the factor *E* is $F_E = 4.40$, and the *F* value of factor *Vcs* is $F_{Vcs} = 9.21$. Because of $F_{0.1}(2,4) < F_E < F_{0.05}(2,4)$ and $F_{0.05}(2,4) < F_{Vcs} < F_{0.025}(2,4)$, it shows that the influencing factor has almost no effect on the change of the amplitude of deposited serpentine fibers and the collector speed has a significant influence on the amplitude of the deposited serpentinr fiber. It can be seen the electric field strength and the collector speed have significantly different effects on the amplitude of the serpentine fibers.

The *F* of factor *E* is $F_E = 10.89$ and the *F* of factor *Vcs* is $F_{Vcs} = 13.74$. It shows that $F_{0.025}(2,4) < F_E < F_{Vcs} < F_{0.01}(2,4)$, which can be indicated the influence of the collector speed is slightly significant, even higher than the electric field strength.

To sum up, by calculating the variance experiment of the serpentine deposition results of the 20# nozzle, it can be seen that the electric potential and the collector speed have different impact on the morphology of serpentine deposits. According to the significant difference of two factors on the morphology of serpentine deposition, it can be obtained more accurately by controlling the experimental parameters. The serpentine deposition data obtained by 25# and 30# Nozzle can be obtained results similar to the variance of 20# Nozzle. Due to the cumbersome calculation, only a summary is made here, and this article will not be performed.

4. Conclusions

In this paper, the influence mechanism of melt electrowriting (MEW) process parameters on the morphology of serpentine fibers is explored by combining the axial bending effect of the jet. The production method of stable and uniform micro-scale serpentine structure fiber is summarized through repetitive experiments.

First, single-factor experiments were performed on the parameters of nozzle diameter, applied voltage, collector speed, and nozzle height. The pattern of the serpentine deposition with the change of parameters is found. Then, according to the electric field strength and collector speed were selected to conduct a multiple coupling factors experiment to explore the significance of the influence of each factor on the serpentine deposition. After the F-test, it has been summarized in this study.

• When the amplitude of serpentine fibers as the mathematical expectation, the electric field strength has almost no effect on the amplitude and collector speed has a significant influence on it.

• When the period of serpentine fibers as the mathematical expectation, the electric field strength and the collector speed have a significant influence on the serpentine deposition.

Micro-scale serpentine structures fibers with great deposition properties have been applied in the flexible electronics manufacturing industry. In the future, with the realization of better serpentine structure deposition and the advancement of functional material MEW technology, micro-scale serpentine structure fibers with specific functions will create new applications. This technology is expected to be applied in the manufacturing of flexible micro-nano functional electronic devices and flexible chip sensors and other high-tech manufacturing.

Acknowledgements

This work was financially supported by National Natural Science Foundation of China (U20A6004).

References

Baji, A. and Abtahi, M. (2013), "Fabrication of barium titanate-bismuth ferrite fibers using electrospinning", *Adv. Nano Res.*, **1**(4), 183-192. http://doi.org/10.12989/anr.2013.1.4.183.

Chinnappan, A., Baskar, C., Baskar, S., Ratheesh, G. and Ramakrishna, S. (2017), "An overview of electrospun nano-fibers and their application in energy storage, sensors and wearable/flexible electronics", *J. Mater. Chem. C*, **5**(48), 12657-12673. https://doi.org/10.1039/C7TC03058D.

Choi, M.K., Yang, J., Kang, K., Kim, D.C., Choi, C., Park, C., Kim, S.J., Chae, S.I., Kim, T.H., Kim, J.H., Hyeon, T. and Kim, D.H. (2015), "Wearable red–green–blue quantum dot light-emitting diode array using high-resolution intaglio transfer printing", *Nat. Commun.*, **6**(1), 1-8. https://doi.org/10.1038/ncomms8149.

Dhanawansha, K.B., Senadeera, R., Gunathilake, S.S. and Dassanayake, B.S. (2020), "Silver nanowire-containing wearable thermogenic smart textiles with washing stability", *Adv. Nano Res.*, **9**(2), 123-131. https://doi.org/10.12989/anr.2020.9.2.123.

Duan, H., Xie, E., Han, L. and Xu, Z. (2008), "Turning PMMA nanofibers into graphene nanoribbons by in situ electron beam irradiation", *Adv. Mater.*, **20**(17), 3284-3288. https://doi.org/10.1002/adma.200702149.

Duan, Y., Ding, Y., Xu, Z., Huang, Y. and Yin, Z. (2017), "Helix electrohydrodynamic printing of highly aligned serpentine micro/nanofibers", *Polymers*, **9**(9), 434. https://doi.org/10.3390/polym9090434.

Fang, F., Chen, X., Du, Z., Zhu, Z., Chen, X., Wang, H. and Wu, P. (2015), "Controllable direct-writing of serpentine micro/nano structures via low voltage electrospinning", *Polymers*, **7**(8), 1577-1586. https://doi.org/10.3390/polym7081471.

Gao, W., Ota, H., Kiriya, D., Takei, K. and Javey, A. (2019), "Flexible electronics toward wearable sensing", *Acc. Chem. Res.*, **52**(3), 523-533. https://doi.org/10.1021/acs.accounts.8b00500.

Huang, L., Wang, H., Zhan, D. and Fang, F. (2021), "Flexible capacitive pressure sensor based on laser–induced graphene and polydimethylsiloxane foam", *IEEE Sens. J.*, **21**(10), 12048-12056. https://doi.org/10.1109/JSEN.2021.3054985.

Huang, S., Liu, Y., Zhao, Y., Ren, Z. and Guo, C.F. (2019), "Flexible electronics: Stretchable electrodes and their future", *Adv. Funct. Mater.*, **29**(6), 1805924. https://doi.org/10.1002/adfm.201805924.

Huang, Y., Bai, X., Zhou, M., Liao, S., Yu, Z., Wang, Y. and Wu, H. (2016), "Large-scale spinning of silver nanofibers as flexible and reliable conductors", *Nano Lett.*, **16**(9), 5846-5851. https://doi.org/10.1021/acs.nanolett.6b02654.

Huang, Y., Ding, Y., Bian, J., Su, Y., Zhou, J., Duan, Y. and Yin, Z. (2017), "Hyper-stretchable self-powered sensors based on electrohydrodynamically printed, self-similar piezoelectric nano/microfibers", *Nano Energy*, **40**, 432-439. https://doi.org/10.1016/j.nanoen.2017.07.048.

Huang, Y., Song, J., Yang, C., Long, Y. and Wu, H. (2019), "Scalable manufacturing and applications of nanofibers", *Mater. Today*, **28**, 98-113. https://doi.org/10.1016/j.mattod.2019.04.018.

Kong, T., Li, J., Liu, Z., Zhou, Z., Ng, P.H.Y., Wang, L. and Shum, H. C. (2016), "Rapid mixing of viscous liquids by electrical coiling", *Sci. Rep.*, **6**(1), 1-8. https://doi.org/10.1038/srep19606.

Kou, L., Huang, T., Zheng, B., Han, Y., Zhao, X., Gopalsamy, K., Sun, H. and Gao, C. (2014), "Coaxial wet-spun yarn supercapacitors for high-energy density and safe wearable electronics", *Nat. Commun.*, **5**(1), 1-10. https://doi.org/10.1038/ncomms4754.

Luelf, T., Bremer, C. and Wessling, M. (2016), "Rope coiling spinning of curled and meandering hollow-fiber membranes", *J. Membr. Sci.*, **506**, 86-94. https://doi.org/10.1016/j.memsci.2016.01.037.

Matsumoto, H., Minami, H., Yamaura, I. and Yoshida, Y. (2019), "Postoperative subdural hematoma with blood flow from an epidural hematoma through a tear at the suture point of an artificial dura substitute", *Acta Neurochir.*, **161**(4), 755-760. https://doi.org/10.1007/s00701-019-03830-7.

Nag, A., Mukhopadhyay, S.C. and Kosel, J. (2017), "Wearable flexible sensors: A review", *IEEE Sens. J.*, **17**(13), 3949-3960. https://doi.org/10.1109/JSEN.2017.2705700.

Nayak, L., Mohanty, S., Nayak, S.K. and Ramadoss, A. (2019), "A review on inkjet printing of nanoparticle inks for flexible electronics", *J. Mater. Chem. C*, **7**(29), 8771-8795. https://doi.org/10.1039/C9TC01630A.

Nezadi, M., Keshvari, H. and Yousefzadeh, M. (2021), "Using Taguchi design of experiments for the optimization of electrospun thermoplastic polyurethane scaffolds", *Adv. Nano Res., Int. J.*, **10**(1), 59-69. http://doi.org/10.12989/anr.2021.10.1.059.

Passieux, R., Guthrie, L., Rad, S.H., Lévesque, M., Therriault, D. and Gosselin, F.P. (2015), "Instability-assisted direct writing of microstructured fibers featuring sacrificial bonds", *Adv. Mater.*, **27**(24), 3676-3680. https://doi.org/10.1002/adma.201500603.

Persano, L., Camposeo, A. and Pisignano, D. (2015), "Active polymer nanofibers for photonics, electronics, energy generation and micromechanics", *Prog. Polym. Sci.*, **43**, 48-95. https://doi.org/10.1016/j.progpolymsci.2014.10.001.

Ramakrishna, S., Fujihara, K., Teo, W.E., Yong, T., Ma, Z. and Ramaseshan, R. (2006), "Electrospun nanofibers: Solving global issues", *Mater. Today*, **9**(3), 40-50. https://doi.org/10.1016/S1369-7021(06)71389-X.

Romagnoli, P., Maeda, M., Ward, J.M., Truong, V.G. and Nic Chormaic, S. (2020), "Fabrication of optical nanofibre-based cavities using focussed ion-beam milling: A review", *Appl. Phys. B Lasers O.*, **126**, 1-16. https://doi.org/10.1007/s00340-020-07456-x.

Shariatpanahi, S.P., Bonn, D., Ejtehadi, M.R. and Zad, A.I. (2016), "Electrical bending instability in electrospinning visco-elastic solutions", *J. Polym. Sci. Pol. Phys.*, **54**(11), 1036-1042. https://doi.org/10.1002/polb.24029.

Wang, X., Xu, L., Zheng, G., Jiang, J., Sun, D. and Li, W. (2021), "Formation of suspending beads-on-a-string structure in electro-hydrodynamic printing process", *Mater. Des.*, **204**, 109692. https://doi.org/10.1016/j.matdes.2021.109692.

Wu, C.C., Reinhoudt, D.N., Otto, C., Subramaniam, V. and Velders, A.H. (2011), "Strategies for patterning biomolecules with dip-pen nanolithography", *Small*, **7**(8), 989-1002. https://doi.org/10.1002/smll.201001749.

Yang, W.M., Zhu, T.K., Jin, Y.A. and Fu, J.Z. (2017), "Facile fabrication of helical microfluidic channel based on rope coiling effect", *Microsyst. Technol.*, **23**(7), 2957-2964. https://doi.org/10.1007/s00542-016-3010-4.

Zhang, C.L., Luo, Y.X., Cheng, R.R. and Wang, X.Y. (2017), "Electromechanical fields in piezoelectric semiconductor nano-fibers under an axial force", *MRS Adv.*, **2**(56), 3421-3426. https://doi.org/10.1557/adv.2017.301.

Zhang, Y.Z., Wang, Y., Cheng, T., Yao, L. Q., Li, X., Lai, W.Y. and Huang, W. (2019), "Printed supercapacitors: Materials, printing and applications", *Chem. Soc. Rev.*, **48**(12), 3229-3264. https://doi.org/10.1039/C7CS00819H.

Zheng, G., Jiang, J., Wang, X., Li, W., Yu, Z. and Lin, L. (2021), "High-aspect-ratio three-dimensional electrospinning via a tip guiding electrode", *Mater. Des.*, **198**, 109304. https://doi.org/10.1016/j.matdes.2020.109304.

Zhu, Z., Chen, X., Huang, S., Du, Z., Liao, W., Fang, F., Peng, D. and Wang, H. (2015), "The process of wavy fiber deposition via auxiliary electrodes in near-field electrospinning", *Appl. Phys. A*, **120**(4), 1435-1442. https://doi.org/10.1007/s00339-015-9330-x.

CC